AT622 Section 7
Earth's Radiation Budget

Here we examine the effects of the atmosphere and clouds on the Earth's radiation budget (ERB). While the notions described deal with the simpler aspects of these effects and are heavily based on TOA observations, the material presented provides important insight into atmospheric radiation. More detailed and rigorous understanding will come when the topics of this section are revisited in later sections in the context of radiative transfer.

7.1 The ERB Measured From Space: An Overview of the ERBE

The history of the ERB measurements closely parallels the overall space effort within the United States and other countries of the world. A reference that details the history of the ERB observation is that of House et al., 1986: History of satellite missions and measurements of the earth radiation budget (1957-1984), *Revs. Geophys,* **24***, 357-377*. Discussion of pre-satellite ERB studies is provided by Hunt, 1986 (same issue of *Rev. Geophys*.). Table 7.1 provides a convenient overview of this history. The first-generation instruments were narrow spectral channel scanning radiometers. These provided spectral radiance measurements for limited ranges of angle. Models of the angular distribution of radiance were required to convert these to flux (via bi-directional models). The second-generation instruments were flat

Table 7.1: Historical Overview.

Satellite Mission	Launch Date	Altitude Range (km)	Inclination Angle (deg.)	Orbit Time	Lifetime(s)	Contributions
First-Generation Missions						
Explorer 7	Oct. 13, 1959	550-1,100	51	Drifter	7 months	First dedicated satellite providing usable ERB data
TIROS 2	Nov. 23, 1960	717-837	48	Drifter	1-5 months	First scanning radiometer with five SW/LW channels
TIROS 7	June 19, 1963	713-743	58	drifter	12 months	Provided 1 year of radiation balance observations
Second-Generation Missions						
Research/ESSA	1960s	≈ 1,500	102	0900/1500	3-15 months	Global data sets from WFOV nonscanning radiometers
Nimbus 3	Apr. 14, 1969	1,100	99	Noon	1 year	Detailed global radiation balance for 1 year
NOAA NOAA-N/NOAA	1970s 1978-1981	≈ 1,500 ≈ 840	102 99	0900 1500/0730	Years Years	Combined data sets provided 10 years of observations
Third-Generation Mission						
Nimbus 7 ERB	Oct. 1978 To the present	950	99	noon	6+ years	Total and spectral solar monitoring; bi-directional reflectance and directional albedo models
Geostationary Missions						
GOES-E/W (75°-135°) METEOSAT ½ (0° longitude)	1970s/1980s 1977/1982	36,000 36,000	0 0	24 hours 24 hours	Years Years	Diurnal variations of SW/LW exitances and cloud distributions: satellite mission simulations

plate broadband instruments that measured a quantity more closely resembling the hemispheric flux (Fig. 7.1) although some deconvolution is required to obtain fluxes. The third generation instrument suite

includes wide field of view, broadband instruments, and narrow field of view scanning instruments. One advantage of the latter is the spatial resolution.

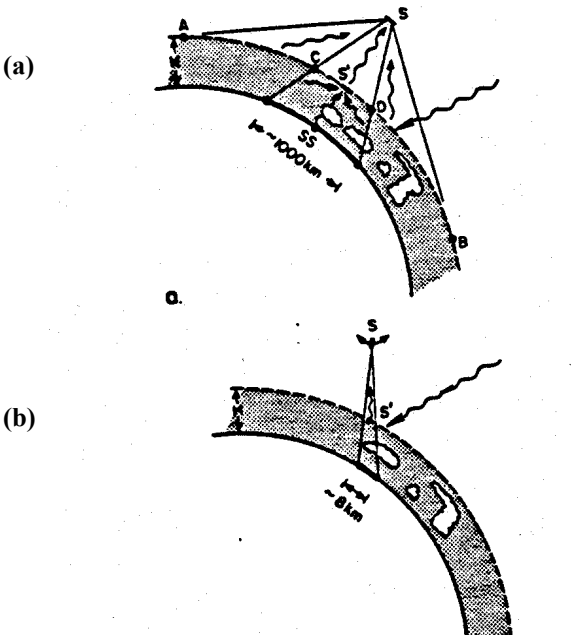

Fig. 7.1 (a) Flat plate instrument versus (b) Scanners.

One of the significant problems of the early studies is the lack of sampling of the diurnal variations. Single satellite missions cannot provide enough observations to pull out the seasonal and diurnal variability at scales varying from the global scale to the synoptic scale to the more localized regional scale. ERBE proposed a three-satellite strategy for sampling the globe (Fig. 7.2a and b) involving two polar orbiters and the ERBS at a 57° inclined orbit. The resulting sampling is given in Fig. 7.2a.

The ERBE instruments are built in two packages: a scanner package and a nonscanner package. The scanner contains three scanning radiometers and capabilities for onboard calibration. The scanner (Fig. 7.3a) consists of a shortwave, longwave, and total radiometer mounted in a single scan head to receive radiation from the same FOV (usually scans across the track). The nonscanner (Fig. 7.3b) contains a total wide FOV (WFOV- view of the entire earth disc) radiometer and a shortwave radiometer. There are also medium FOV radiometers (MFOV) and an active cavity radiometer to measure solar output.

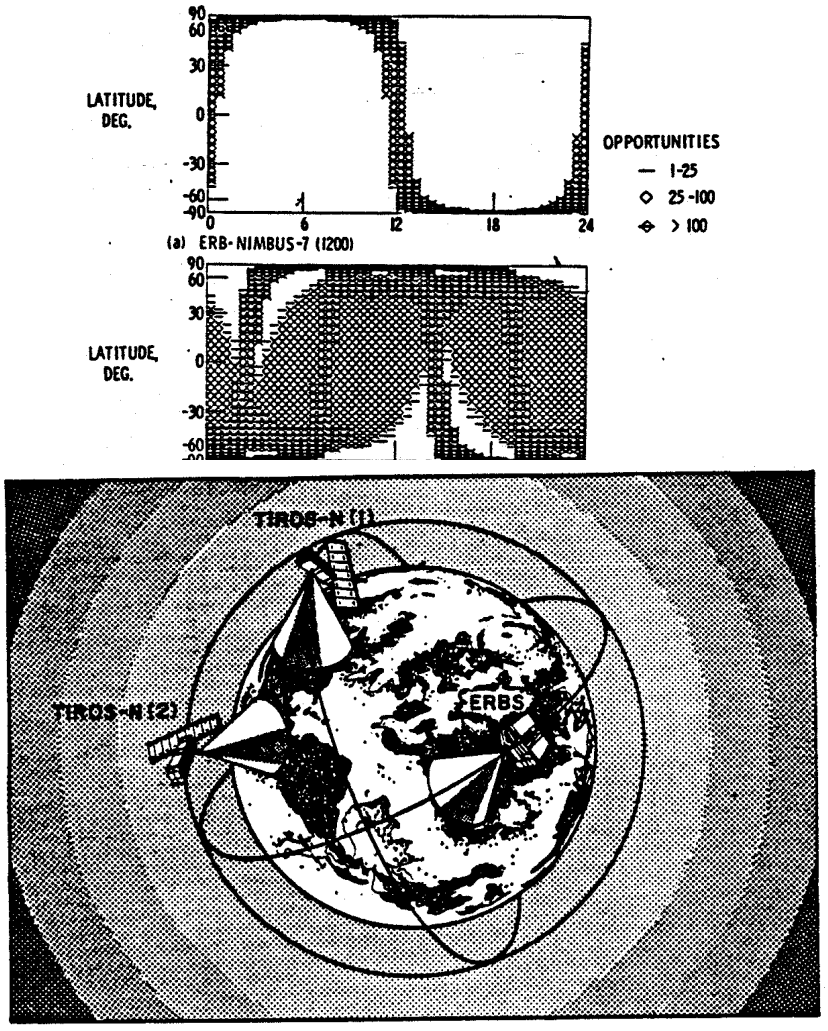

Fig. 7.2 (a) Local time coverage of Nimbus 7 satellites upper and the three satellites combined (lower). (b) The three satellite orbit configurations.

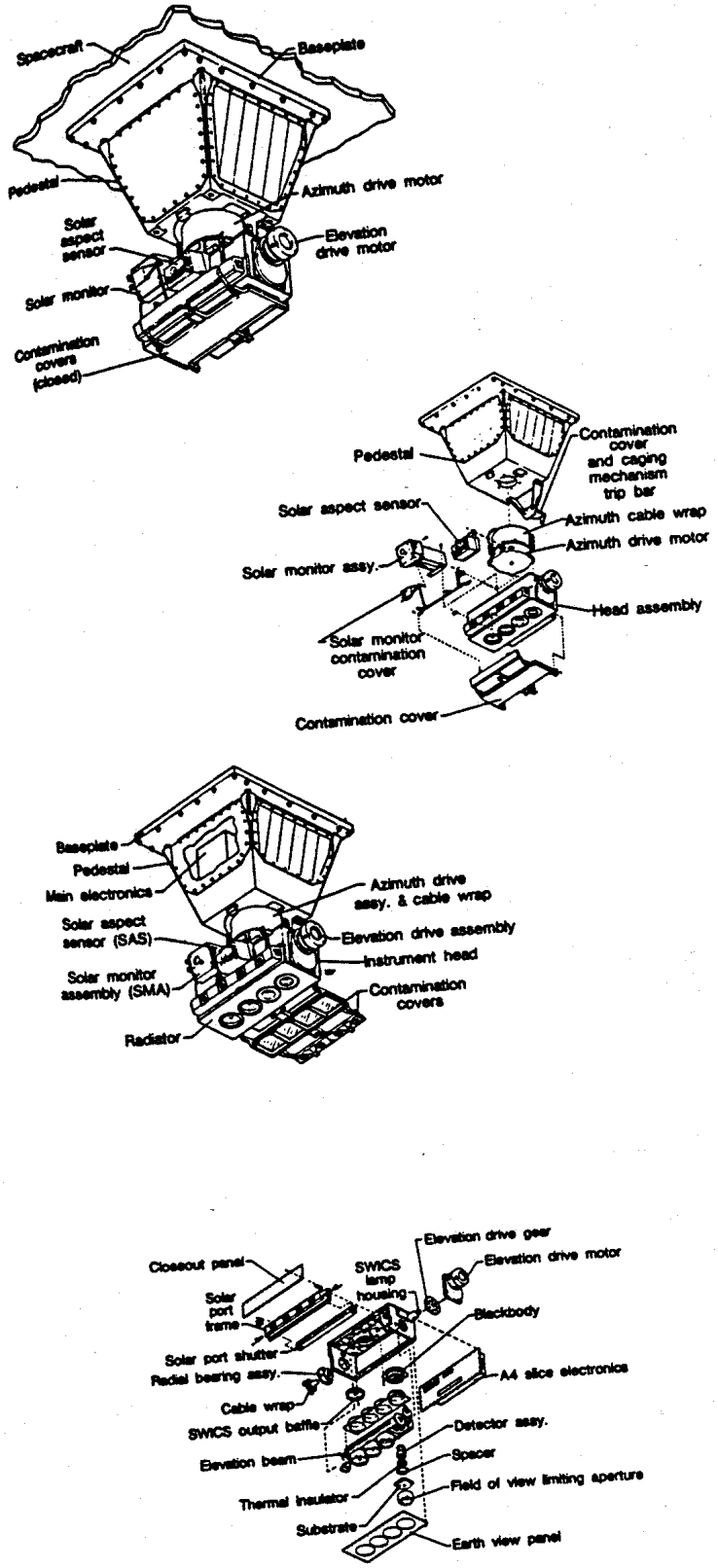

Fig. 7.3 (a) Scanning radiometer. (b) Nonscanning radiometer.

7.2 Satellite Classification of Clouds

Clouds provide a first-order effect on the radiative budgets and water exchanges in the atmosphere. They also play a fundamental role in studies of climate and climatic change. Several attempts have been made to classify the global distribution of clouds based on measurements obtained from radiometers flown on satellites. Two examples of these radiometric classifications of clouds will now be discussed.

(a) Emission Classification in the Split Window

Inoue (1989) developed a simple way to classify clouds according to the difference in their emission properties at 11 and 12 μm. As mentioned earlier, $\Delta T = T_{10.8} - T_{12}$ is a good indicator of the opacity of clouds. Thick clouds, radiating approximately like a blackbody, possess small values of ΔT whereas thin clouds exhibit more variable values of ΔT as described earlier in a way that depends on particle size and other factors.

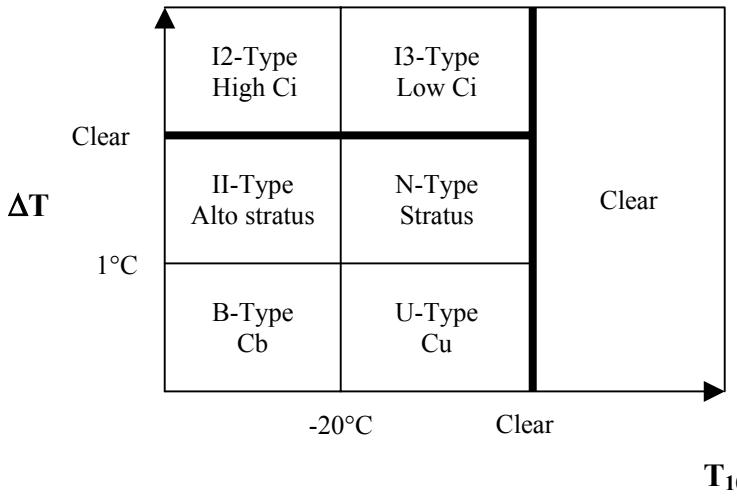

Fig. 7.4 An example of a cloud-type classification diagram introduced by Inoue (1989).

Inoue's classification scheme is based on threshold analyses of the T - ΔT diagram like that shown in the example shown in Fig. 7.4. Two threshold values of ΔT can be identified, one at ΔT = 1 K corresponding to optically thick clouds and another to a slightly larger value corresponding to the clear sky value of ΔT. Two threshold values of the brightness temperature $T_{10.8}$ are also introduced in the Inoue scheme; one is the high cloud threshold, which is set at -20°C, and the other corresponds to clear sky temperatures. Data representing different cloud types fall in the different classification boxes. For example, cumulonimbus clouds are thick, possess ΔTs less than 1 K, and are cold. These fall in the type B category. Low level cumulus and stratocumulus clouds fall into Inoue's category U. Thin cirrus clouds are characterized by values of ΔT that exceed the clear sky threshold value and fall in categories 12 and 13 for thick and thin clouds, respectively. Stratus clouds have opacities between cirrus and cumulus clouds, and fall into categories II and N.

(b) The International Satellite Cloud Climatology Project (ISCCP)

ISCCP formerly began in 1983 with the collection of the first internationally coordinated satellite intensity data. The original plan called for this collection for only a five-year period but the ISCCP extended this collection to 1995. This program was the first of its kind involving routine collection of

operational satellite data. Many key problems needed attention including lack of global converge and cross calibration of satellite radiometers. These issues are addressed elsewhere.

The cloud detection scheme used in ISCCP is different from the emission scheme highlighted above as it uses both visible reflection information as well as emitted radiation. The detection approach examines all of the data for one month to collect statistics on the space/time variations of the VIS and IR intensities. The key assumptions used in the analysis are that the intensities in clear scenes are less variable than those in cloudy scenes and that it is the clear scenes that compose the darker and warmer parts of the VIS and IR intensity distributions, respectively. Estimates of the clear sky values of VIS and IR intensities for each location and time are made and composited into maps (these are referred to as the "clear sky composites"). This approach is novel in two respects. First, all of the complicated tests usually used to detect cloudiness directly, many of which were first proposed by other investigators, are used here to identify clear scenes. The use of time variations at one location to identify clear scenes also differs from many other methods.

The differences between the intensities measured and the estimated clear sky intensities are compared to the uncertainties in estimating the clear intensities. If the differences are larger than this uncertainty and in the "cloudy direction" at either wavelength (colder IR or brighter VIS), then the pixel is labeled cloudy. Once each pixel is classified as clear or cloudy, the measured intensities are compared to radiative transfer model calculations that include the effects of the atmosphere, surface and clouds. The intensity data are then converted into two-cloud properties—the "visible" optical thickness (defined at 0.6 μm) and a cloud-top pressure. The optical thickness parameter determines the amount and angular distribution of sunlight reflected by the cloud layer (the full effects of multiple scattering are included in the model and we will examine the form of this model later)—the cloud-top pressure is supposed to account for cloud emissivities less than 1. At night, when only IR intensities are measured, no cloud optical thickness is reported and IR variations are associated with the cloud-top brightness temperature.

Thus, the ISCCP clouds are categorized in terms of cloud-top pressure and optical-depth properties as schematically shown in Fig. 7.5a. A second category group, based on a combination of those in Fig 7.5a, is given in Fig 7.5b. Two examples of the two-dimensional categories as defined in Fig. 7.5a for July 1983 are presented in Figs 7.5c and d for two different latitude zones. Maps of the categories introduced in 7.5b are shown later in Fig. 7.9. In the subtropics during winter (Fig. 7.5c), the predominant cloud type has low tops and relatively low optical depths (probably associated with highly broken cloud). The tropical distribution is more complicated showing a prevalence of high, optically thick clouds and low, relatively thin clouds associated with highly broken low-level clouds.

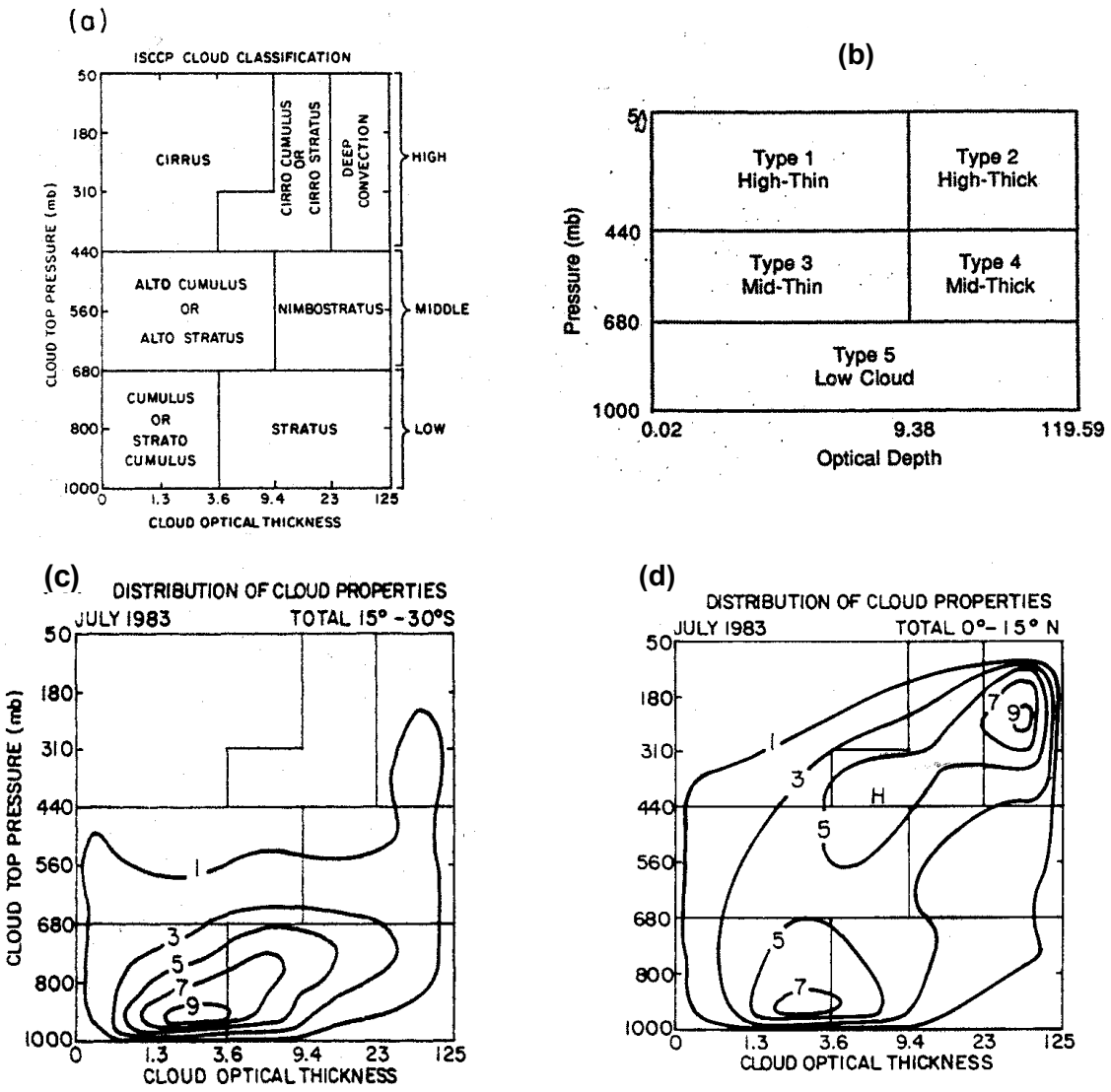

Fig. 7.5 (a) Radiometric classification of cloudy pixels in terms of optical thickness and cloud-top pressure. (b) A second category group based on a combination of those in (a). (c) The frequency distribution of cloud optical thickness and cloud-top pressure for July 1983 for the southern subtropics and (d) the northern tropics (from Rossow and Shiffer, 1991).

7.3 The Effects of Clouds on the ERB: The Idea of Cloud Radiative Effect

Our every day experience tells us that clouds are white and reflect significant amounts of solar radiation. Conversely, clouds are dark at infrared wavelengths, strongly absorbing and hence also strongly emissive. These characteristics are used to detect clouds in the ISCCP algorithm. What we will learn in later sections is that the ability of clouds to reflect solar radiation is related to their ability to emit radiation in a complex manner. When viewed from the top of the atmosphere, clouds produce a curious impact on radiative transfer, on the one hand increasing (solar) radiation leaving the planet, yet on the other hand inhibiting the emission of (infrared) radiation to space by absorbing radiation emitted from below and replacing it with a reduced amount of radiation emitted by the colder cloud particles

themselves. These two competing processes produce a net effect that is in somewhat delicate balance—a balance that depends on height, thickness, amount of clouds, and even on the size of the particles in the cloud that governs the ability of cloud particles to scatter and absorb radiation.

Example 7.1: Golden Arches

One of the advantages of satellites as observational platforms of clouds is their ability to record patterns and structures of clouds over wide ranges of space and time. A method that exploits this particular advantage, as well as using the properties of cloud emission, is the spatial coherence technique introduced by Coakley and Bretherton (1983). The idea behind the approach is portrayed in the upper panel in Fig. 7.6. It schematically shows a group of 2 x 2 neighboring pixels of 11 μm radiances expressed in this specific example as brightness temperature. These pixels are processed to provide the average 11 μm brightness temperature of the group and the standard deviation about this average. The latter is a measure of the texture of the image on the scale of the pixel array chosen. These two pixel group quantities are then plotted on a scatter diagram in the fashion given by Fig. 7.6. The satellite data used to construct this scatter plot are the 11 μm radiances obtained with the NOAA-9 overpass at 2242 GMT on July 7 obtained from the AVHRR viewing marine stratus clouds off the west coast of California (Coakley, 1991).

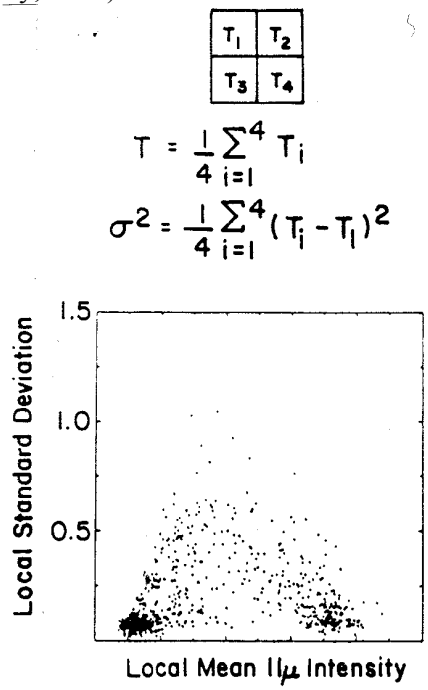

Fig. 7.6 A schematic demonstration of the method of spatial coherence (upper panel) as it might be applied to brightness temperatures. Spatial coherence analysis of 11 μm intensities for a (250 km)^2 region over stratus clouds off the west coast of California. Each point represents values for a 4 x 4 array of (1 km)^2 AVHRR pixels (Coakley, 1991).

Example 7.1: Continued.

The scatter of points on the diagram resembles an arch. The feet of the arch contain important information about those regions of the image that are relatively homogeneous across the group of neighboring pixels. One foot is associated with the relatively clear sky portion of the scene and the other to the pixel groups that are completely filled by a cloud with the same temperature. This provides a way of discriminating clear sky brightness temperatures from partially cloudy skies (T_{broken}) and from the brightness temperature (T_{cld}) of a homogeneous layered cloud. For the case shown, only two effectively homogeneous surfaces exist, one is the clear sky background and the other is that of the solid cloud portions of the image. The point in the arch corresponds to a partially filled pixel group of cloud cover N. This approach relies on the statistical nature of the observations that can be used to identify both T_{clr} and T_{cld}.

We consider and refer to the two largely compensating effects as follows:

- The albedo effect—clouds reduce the net solar input into the planet by reflecting more solar radiation to space. This is also sometimes referred to as a cooling potential of the planet.
- The 'greenhouse' effect—clouds reduce the longwave output by effectively raising the level of emission to levels specified by colder temperatures.

A graphic example of these two processes, manifested in the ERB, is shown in Fig. 7.7 in which the annual cycle of the ERB quantities of α, F_{∞}, and F_{net} are presented for a region of the Asian monsoon. What is remarkable is how nearly complete is the cancellation of these opposite effects. The fundamental question is do these effects cancel globally or does one component dominate over the other?

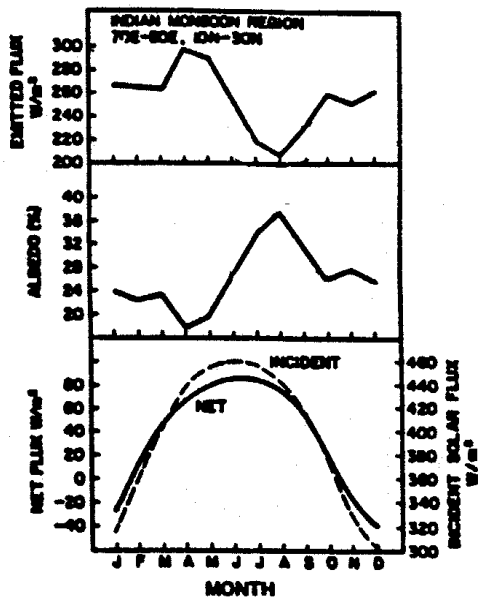

Fig. 7.7 The annual cycles of α, F_{∞} and F_{net} for the Asian monsoon region indicated.

(a) The Cloud Radiative Effect

One way of studying these compensating radiative processes on the ERB is in terms of a comparison between the TOA fluxes in cloudy portions of the atmosphere to equivalent fluxes in clear skies. Flux difference quantities derived in this way are often mistakenly thought of as the measure of a forcing applied to the Earth-atmosphere system by radiative processes of clouds. As we will see it is not, but these quantities do serve as a useful and helpful diagnostic of the effects of clouds on the ERB. Unfortunately, these diagnostics do not provide the insight needed to determine just what properties of clouds govern these effects although we will hint at these governing properties here and return to these later.

The flux difference quantities are introduced as follows. Suppose for the moment the shortwave component of the reflected radiation can be written as

$$F_s\,(\text{observed}) = F_s\,(\text{clear})\,(1 - N) + NF_s\,(\text{cloudy}) \tag{7.1}$$

where N = cloud amount, F_s (clear) is the radiation reflected by the clear sky portion of the atmosphere and F_s (cloudy) is that flux associated with reflection from the cloudy skies. It should be stressed that we use Eqn. (7.1) only to fix ideas as a relationship such as this and has no theoretical basis. Ignoring this with rearrangement

$$\begin{aligned} F_s\,(\text{observed}) &= F_{clear} + N\overbrace{(F_{cloudy} - F_{clear})}^{-C_{SW}} \\ C_{SW} &= F_s\,(\text{clear}) - F_s\,(\text{observed}) < 0 \end{aligned} \tag{7.2}$$

The quantity C_{SW} refers to the specific contribution to the ERB by reflection from clouds. It can be derived independent of the dubious assumptions of Eqn. (7.1) provided we know the clear sky flux. In going from Eqn. (7.1) to Eqn. (7.2) we can think of C_{SW} as containing a factor due to how much cloud exists (i.e., N) and a factor that defines how readily clouds reflect sunlight when they exist. The flux quantity C_{SW} is negative by convention since clouds increase the reflection to space relative to clear skies.

Using entirely similar arguments

$$C_{LW} = F_\infty\,(\text{clear}) - F_\infty\,(\text{observed}) > 0 \tag{7.3}$$

is the effect of clouds on the longwave component. As noted, this component generally exceeds zero as a result of reduced emission from colder clouds. The net effect of clouds is

$$C_{net} = C_{SW} + C_{LW} \tag{7.4}$$

(b) ERBE Results of Cloud Effects

Once clear sky fluxes are derived, then C_{SW} and C_{LW} readily follow. Examples of these flux difference quantities are shown in Fig. 7.8. Monthly average fluxes derived from ERBE are composited together to produce JJA and DJF maps of C_{LW}, C_{SW}, and C_{net}. Features of most relevance to note are:

- Longwave cloud forcing is a measure of the reduction by clouds of the longwave radiation emitted to space; hence it is a measure of the greenhouse effect of clouds. Clouds reduce emission to space because at their bases they absorb radiation emitted by the warmer surface and at their tops they emit to space at colder temperatures. Deep cold clouds such as occur as part of the monsoon cloud systems over the Indian Ocean and Indonesia have the largest greenhouse effect.

- Because clouds reflect more shortwave solar radiation than the adjacent clear skies, the shortwave forcing is negative—a 'cooling' effect. Surprisingly, the magnitude of this effect is almost precisely as large as the longwave forcing over the tropical cloud systems, and is even larger than the longwave effect over the mid- and high-latitude oceans in the summer hemisphere.
- The net cloud radiative forcing (shown as the bottom panel) is the sum of longwave and shortwave cloud forcing. The averages range from -100 to –140 W m^{-2} (dark blue) to 10-40 W m^{-2} (red). The net globally averaged effect is largely negative; hence clouds overall act to cool the planet (see Tables 7.2 and 7.3). The strongest cooling is caused by the persistent maritime stratus off the west coast of continents and storm-track clouds in the summer hemisphere over the mid- and high-latitude Atlantic and Pacific Oceans.

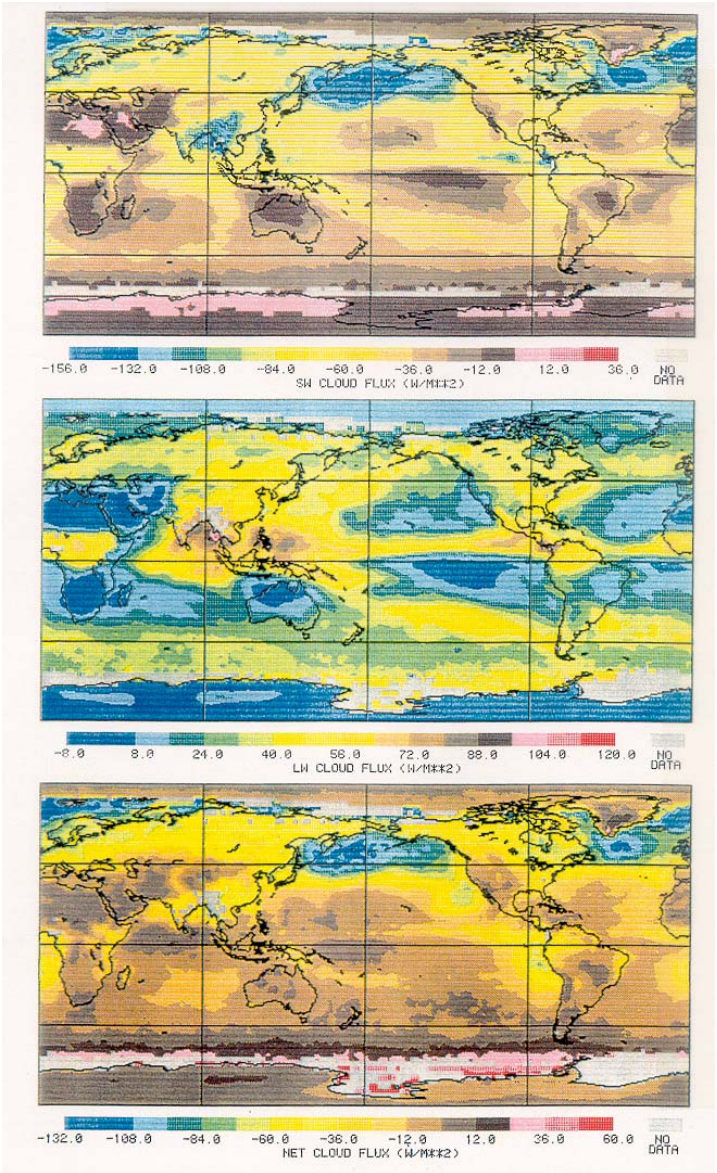

Fig. 7.8 Cloud radiative forcing for JJA 1985 (scales expressed in W m^{-2}).

Because the effects of clouds on C_{LW} and C_{SW} are largely reciprocal, processes that affect one component by a disproportionate amount offers greatest potential for significantly influencing the ERB and thus the Earth's climate. We will study some of these processes later in this course and return to this reciprocity in Section 7.6.

Table 7.2 Nimbus 7 cloud short, long, and net radiative forcing (W m^{-2}). ERBE estimates are in parentheses for middle month of the three-month cycle.

	C_{SW}	C_{LW}	C_{net}
JJA	-42.1 (-46.4)	24.4 (30)	-17.6 (-16.4)
SON	-44.0 (-45.2)	24.5 (32)	-19.4 (-17.4)
DJF	-44.6 (-44.6	22.2 (30.6)	-22.4 (-21.3)
MAM	-44.7 (-44.7)	25.2 (31.3)	-19.5 (-13.2)

Table 7.3 Contributions to flux effects by type.

	Type 1 high, thin		Type 2 high, thick		Type 3 mid, thin		Type 4 mid, thick		Type 5 low		
	JJA	DJF	JJA	DJF	JJA	DJF	JJA	DJF	JJA	DJF	Sum Average
Ni	10.2	10.0	8.5	8.8	10.7	10.7	6.5	8.2	27.2	25.9	63.3
OLF	6.5	6.3	8.4	8.8	4.8	4.9	2.4	2.4	3.5	3.5	25.8
Albedo	1.2	1.1	4.1	4.2	1.1	1.0	2.7	3.0	5.8	5.6	14.9
Net	2.4	2.3	-6.4	-7.5	1.4	0.8	-6.6	-8.5	-15.1	-18.2	-27.6

7.4 Classification of Cloud Effects in Terms of Cloud Type

Ockert-Bell and D. L. Hartmann (OBH), 1992: The effect of cloud type on earth's energy balance: results for selected regions, *JGR*, **86**, 9739-9760.

In this study, the effects of different cloud types, as defined by ISCCP are regressed with ERBE data. For convenience, a reduced cloud category was introduced (Fig. 7.5b) and the 1985/86 DJF and 1986 JJA distributions are also shown in Figs. 7.9a and b for reference. High cloud types occur preferentially where convection occurs in the tropics and in mid-latitude storm tracks. High thick clouds occur over a smaller portion of these areas than high thin clouds. Low clouds appear to be predominantly oceanic and most abundant in the eastern subtropical oceans where the SST is relatively low and the mean vertical motion is downward. Total cloud cover is greatest over the high-latitude ocean where stratus regimes are well developed and in regions of intense tropical convection.

To isolate the contribution of each cloud type to the TOA ERB cloud flux effect, OBH uses a simple regression analysis of the form

$$R = a_0 + \sum_{i=1}^{5} a_i N_i \tag{7.5}$$

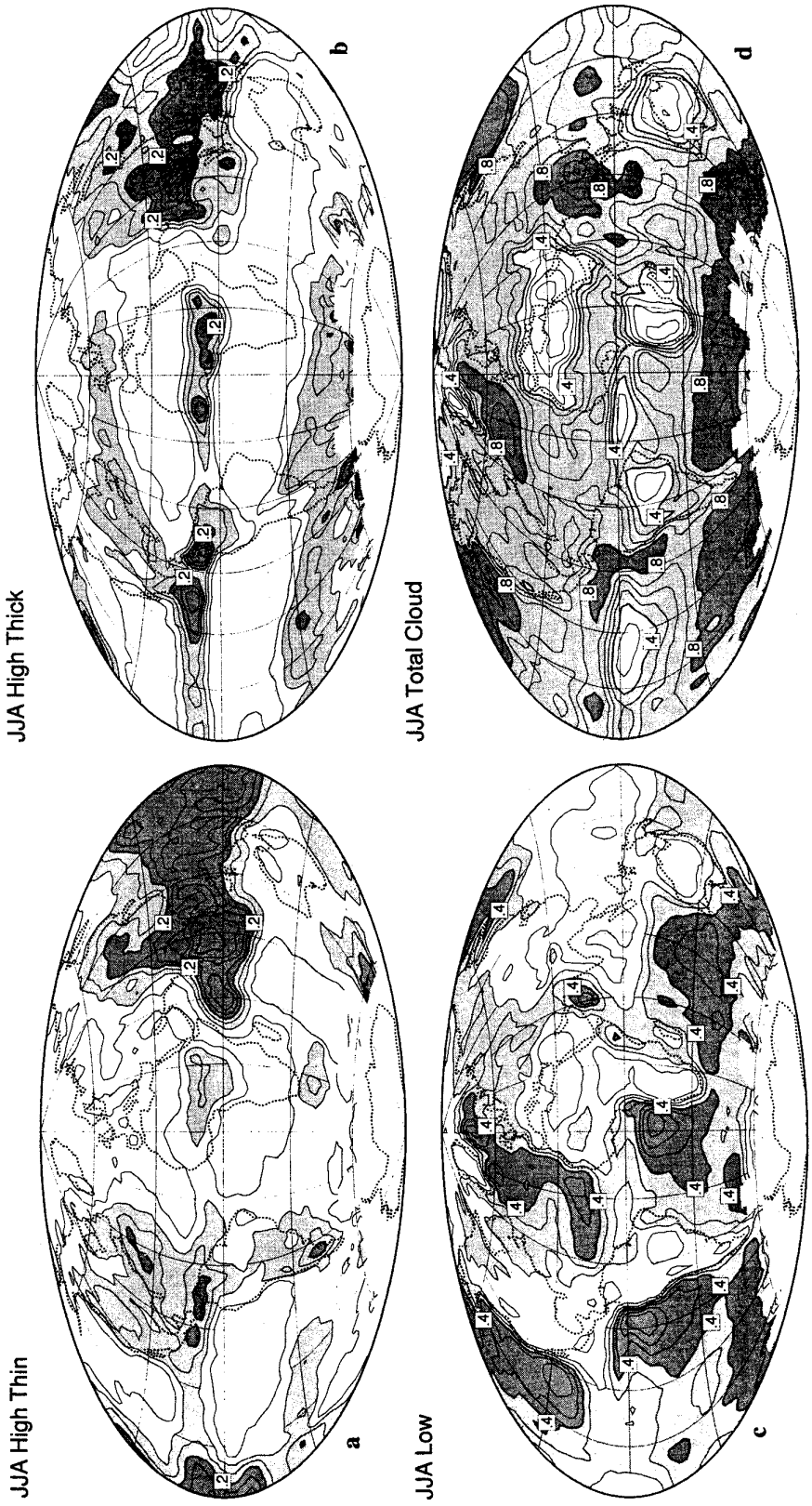

Fig. 7.9a Geographic distributions of the cloud fraction as given by the categories of Fig. 7.5b for the JJA season of 1996. Missing values occur where insolation is small.

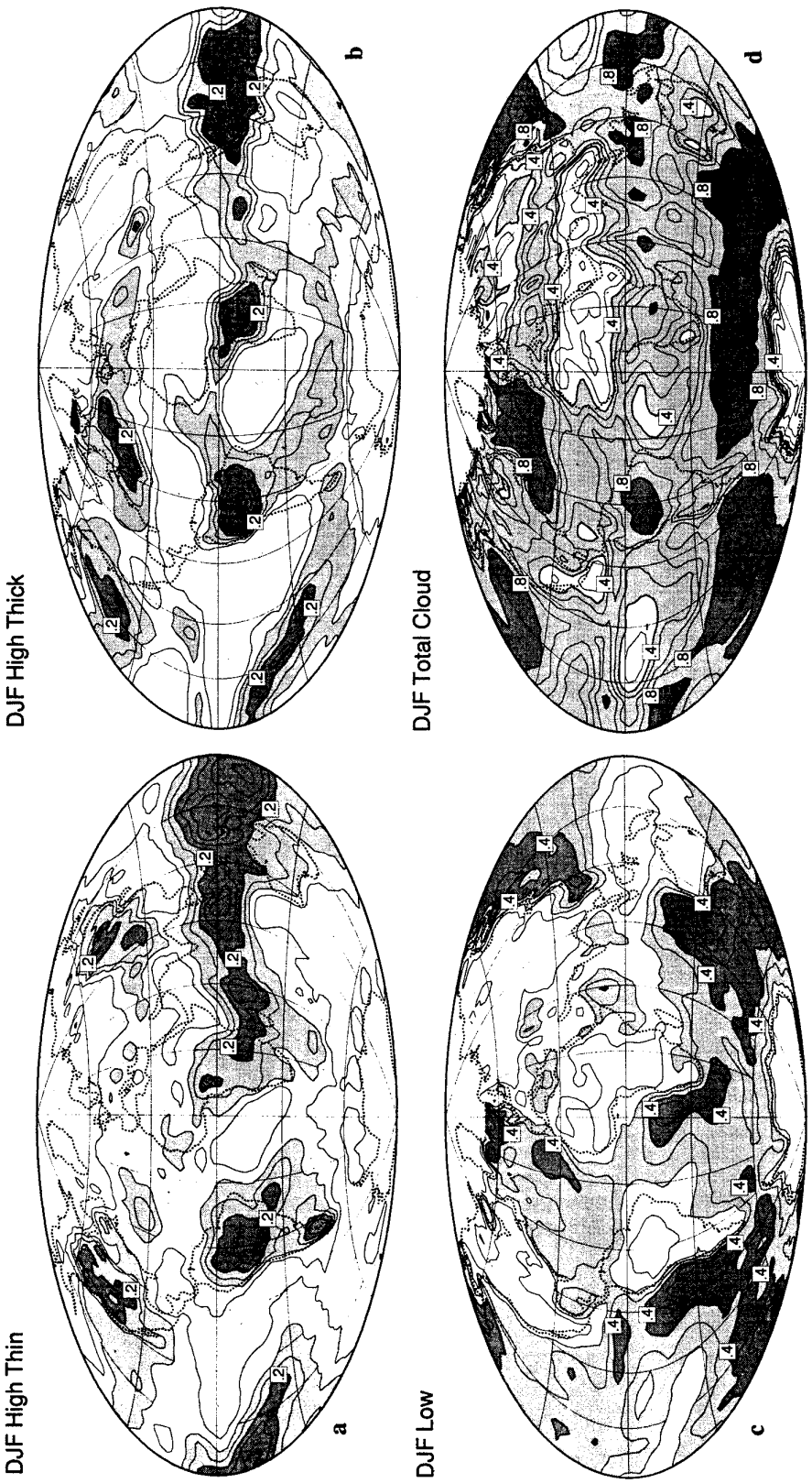

Fig. 7.9b As in (a) but for DJF 1995/1996.

where R is the relevant flux quantity of interest (the net flux, OLR or albedo), N_i is the fractional cloud coverage by type i and a_i is the coefficient of the regression. If this regression approximates the effect of cloud on radiation, its interpretation is as follows

$$R = R_{clear} + \sum_{i=1}^{5} \Delta R_i N_i \tag{7.6}$$

where $R_{clear} = a_0$ is the radiation flux in the absence of clouds and ΔR_i is the change in radiation associated with overcast cloud of type i. This interpretation does depend on how well the data fit this equation (e.g., if the scene is overcast most of the time it will be difficult to deduce the intercept a_0).

Figure 7.10a, b and c shows zonal average values of the OLR flux difference, the shortwave flux differences, and the net flux difference derived as the sum for all cloud types (i.e., the curves labeled ISCCP are the summation terms of Eqn. (7.6)) compared to the flux differences formed from ERBE data. ERBE values suffer in regions where persistent overcast conditions prevail and the differences between the two estimates tend to be greatest in these regions, particularly poleward of 60°S.

The contributions by cloud type are more easily seen in Fig 7.11a, b and c. From these diagrams we note:

- Highest clouds contribute most to the longwave flux effect (type 1 and 2 of Fig. 7.5b) although middle and low clouds contribute in high latitudes.
- The largest effect on shortwave fluxes comes from thicker high clouds in the tropics and low clouds in mid-to-high latitudes. Optically thin clouds (type 1 and 3) contribute little.
- The largest contributions to the net flux difference are provided by low clouds especially through their effect on solar radiation in the summer hemisphere.

The flux differences by type are given in Table 7.3. The longwave effect is about 26 W m^{-2}, some 5 W m^{-2} lower than the ERBE value of 31 W m^{-2}. The albedo effect is about 15% for both ISCCP and ERBE but the net flux of -27 W m^{-2} is more negative than the ERBE value by approximately 10 W m^{-2}.

7.5 Other Relations

(a) SST

The C_{LW} provides a direct measure of the reduction of longwave radiation by absorption and emission of clouds in the atmosphere relative to clear skies. Figure 7.12a presents 12 months of C_{LW} derived from ERBE data as a function of SST and compares the same flux quantity derived from the CSU GCM. The general behavior of C_{LW} with SST appears to show two distinct regimes of behavior; in one regime, C_{LW} decreases over much of the SST range varying from values of 40 W m^{-2} at $T_s \approx 273$ K to about 0-10 W m^{-2} at $T_s \approx 300$ K. The second regime occurs over water warmer than about 300 K, where C_{LW} dramatically increases to values near 80 W m^{-2}. This behavior is partly indicative of the increased cloudiness both equatorward and poleward of the subtropics, which are indicated on this diagram by the minimum in C_{LW}, and partly a result of the changing macroscopic properties of clouds in these regions where cold deep clouds prevail over the warmer equatorial regions and give rise to the largest values in C_{LW}. The comparison between the simulated relationship and that observed suggests that these two regimes are actually well simulated by the model although the magnitudes of C_{LW} over the warm ocean regime are larger than observed and slightly smaller than observed over colder waters. Two possible sources for the discrepancy over the warmest SSTs may be related to specific assumptions in the model

regarding how clouds are treated. The assumption that anvil clouds radiate as a blackbody together with the assumption that clouds completely fill the grid box will exaggerate the model values of C_{LW} over the warm SST regions.

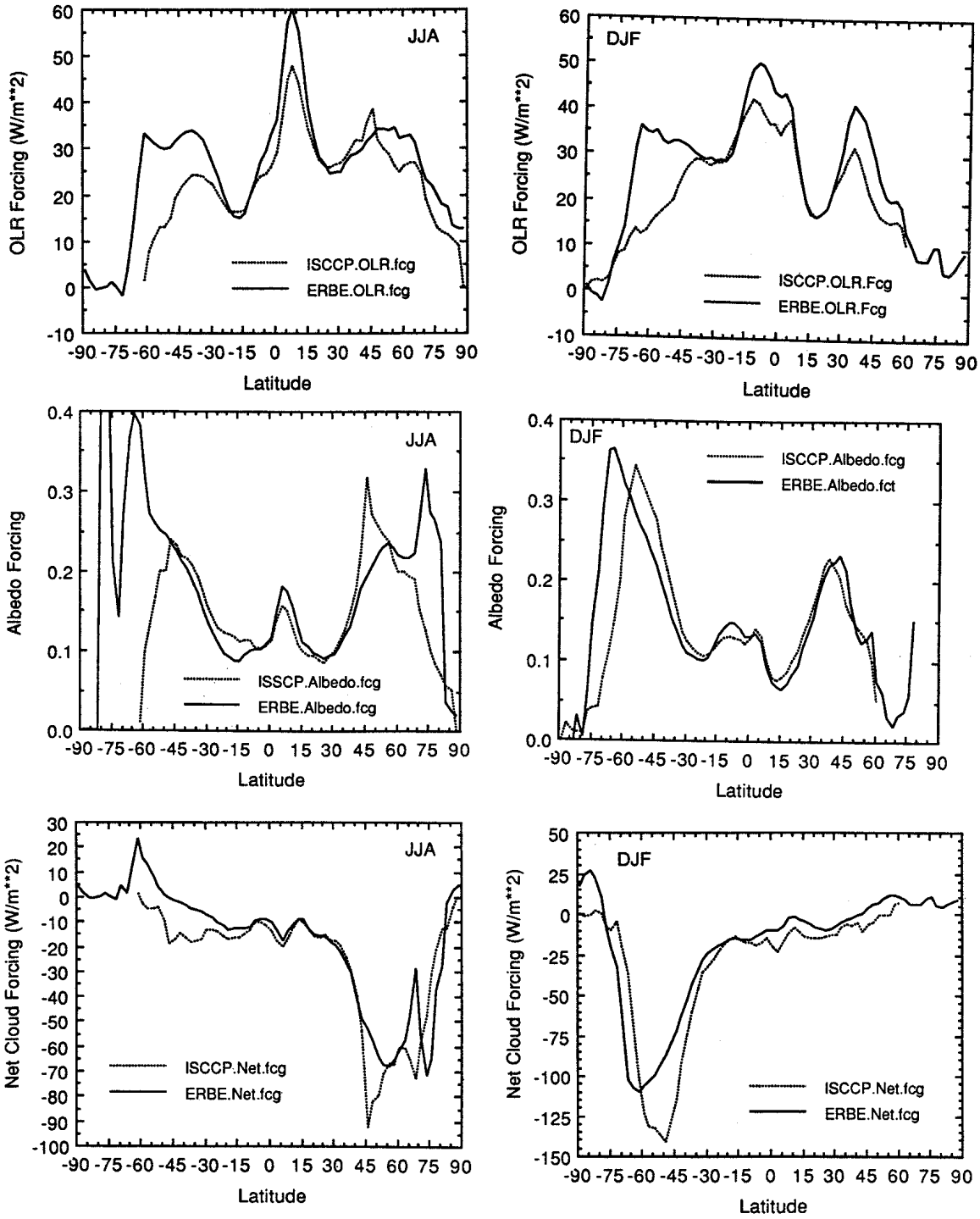

Fig. 7.10 Zonally averaged C_{LW}, C_{SW}, C_{net} derived from the ERBE-ISCCP regression and compared to ERBE quantities.

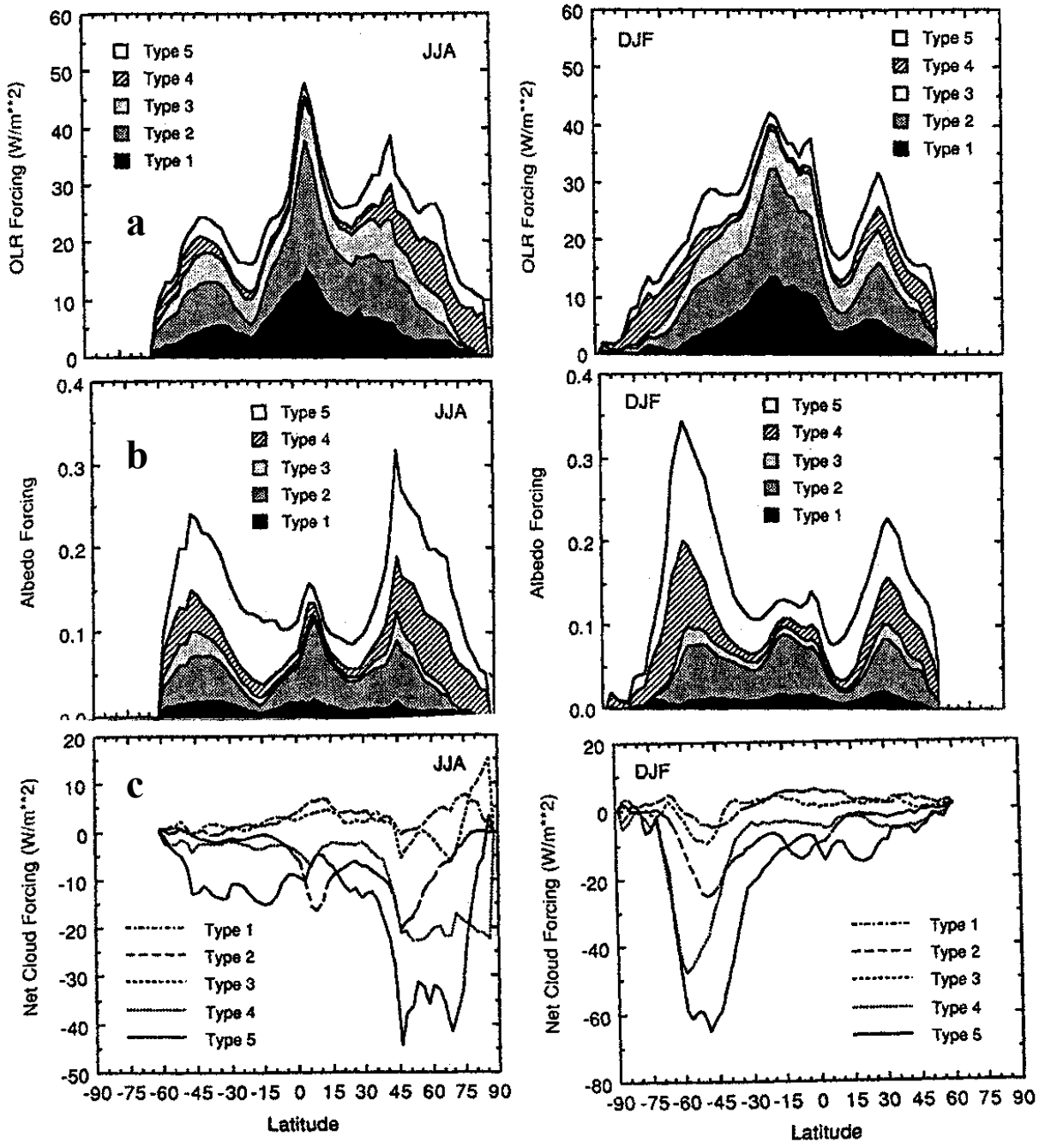

Fig. 7.11 Zonally averaged cloud radiative OLR (a) by cloud category and albedo difference (b), and (c) net flux differences.

Figures 7.12b shows the January and July values of C_{SW} as a function of SST. Values for each hemisphere are shown separately to highlight the complicated variation of C_{SW} with SST. The solar fluxes reflected by the summer hemisphere clouds vary with SST in a way that resembles the two regimes noted for C_{LW}, except that C_{SW} increases from about -150 W m^{-2} for the colder SST's (and thus at higher latitudes) due to the reflection from the summertime clouds located in the mid- to high-latitude storm tracks. C_{SW} increases to near zero over the subtropics, followed by a sharp decrease associated with the

bright clouds of the warmer equatorial oceans. The behavior of C_{SW} in the winter hemisphere poleward of the subtropics differs from that just described for the summer hemisphere. In the former case, the variation of C_{SW} with SST is a result of the product of two factors that have opposing variations with latitude; one is the decreasing insolation and the other is the increasing albedo with increasing latitude. The latter, in turn, is a result of both increasing cloudiness poleward of the subtropics and the decreasing solar elevation with increasing latitude. Both factors contribute to an increase in the albedo, of cloud from the subtropics to mid-latitudes as we show below. The two factors, that of an increased albedo and that of a decreasing solar flux, combine to produce a variation in C_{SW} that starts near zero for clouds at high latitudes and decreases to a minimum of -50 W m^{-2} at approximately T_s = 293 K, followed by an increase towards zero and then a rapid fall off with increasing SST, similar to that noted for the summer hemisphere.

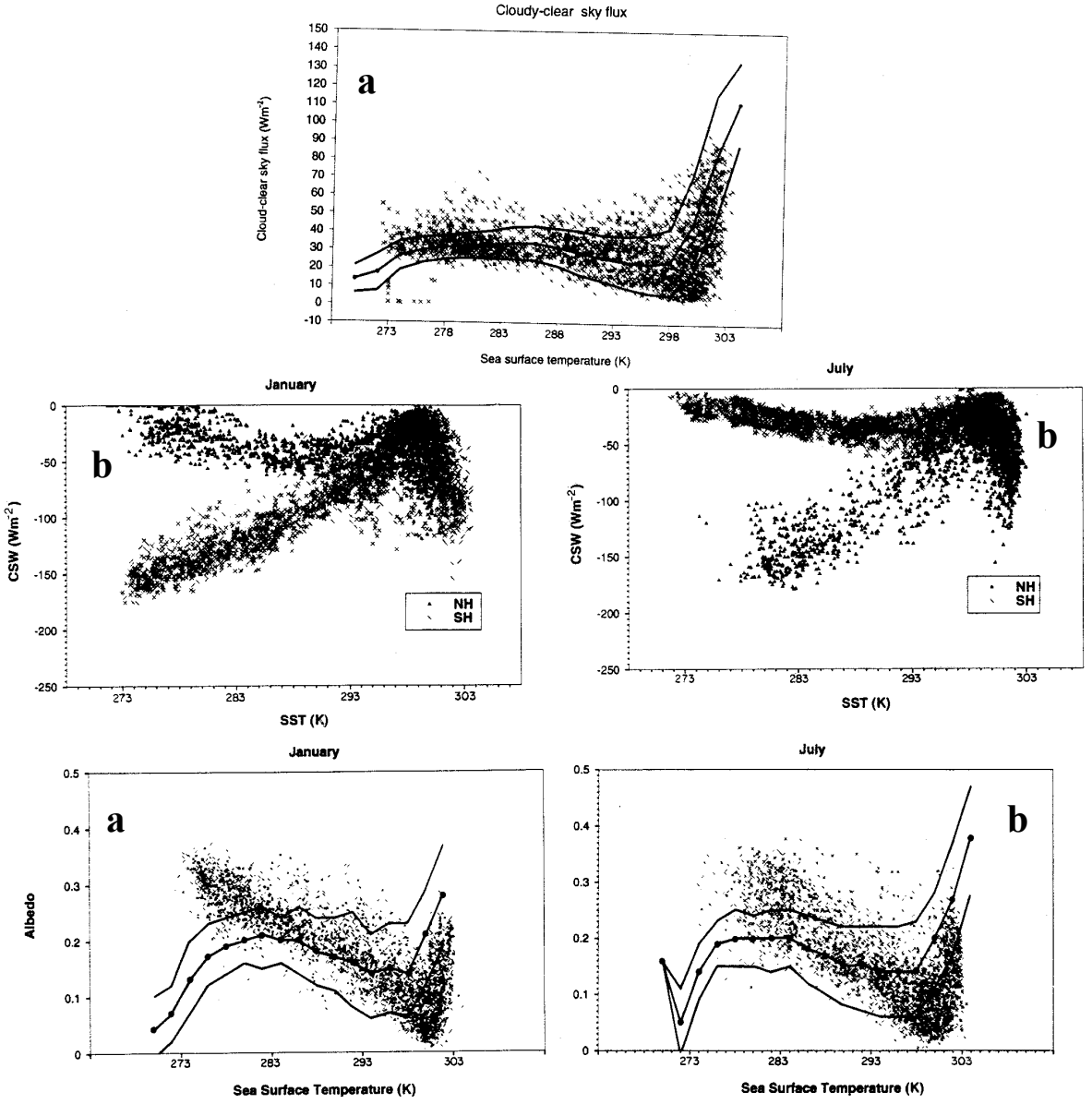

Fig. 7.12 (a) C_{LW} as a function of SST. (b) January and July C_{SW} as a function of SST. (c) Same as for (b) but albedo ($\Delta\alpha = 4C_{SW}/Q_{\odot}$) as a function of SST. Lines indicate CSU GCM model results.

Figure 7.12c presents January and July values of $\Delta\alpha$ as a function of SST. The remarkable feature of these diagrams is how the different hemispheric behavior of C_{SW} maps onto one broad and apparently well-defined relationship. The albedo parameter $\Delta\alpha$ has a minimum over the subtropics where there is a minimum in cloudiness and increases both equatorward and poleward of these clear sky regions. The SST-$\Delta\alpha$ relationships obtained from the GCM are also given on these diagrams for comparison. The model behavior of $\Delta\alpha$ with SST broadly follows the observed behavior, although there are significant differences between the two sets of data. The cloud albedo predicted by the model exceeds that observed in the equatorial warm ocean regions but is much too low for the mid-latitude clouds over regions characterized by $T_s < 285$ K. These features may be due to poorly modeled cloud amount, poorly specified cloud albedo, or a combination of both (note that $\Delta\alpha$ is a hybrid of both factors). Comparisons conducted by Harshvardhan et al. (1989) between the total cloudiness of the model versus the ISCCP total cloudiness reveals that the model tends to overpredict cloudiness in the subtropics (hence the larger values of $\Delta\alpha$ at temperatures near 300 K), slightly underpredicts the total cloudiness in the equatorial regions and greatly overestimates the cloudiness in the summer mid-latitudes. This suggests modeling problems both with the parameterization of cloud albedo in the equatorial region and with estimating the effect of cloud amount on the subtropics and higher latitudes on albedo.

(b) Relation to Liquid Water

We will learn later the importance of the cloud water (and ice path) to the bulk radiative effects in clouds. In fact, it is shown that the liquid and ice water paths are directly related to the cloud optical depth. Global cloud liquid water information is presently derived from the microwave radiance data obtained from the SSMI operational instrument (e.g., Greenwald et al., 1993). From these data, we hope to establish a better understanding of the links between liquid water path, temperature and radiative properties of clouds. For example, Fig. 7.13a presents the results of the correlation between LWP and atmospheric temperature much in the way cloud optical depth and temperature were correlated in the study of Tselioudis et al. (1992). Figure 7.13a presents the parameter

$$f = \frac{d \ln W}{T} \tag{7.7}$$

derived from gridded LWP data. The clouds used to define this parameter correspond to ISCCP defined low clouds and the liquid water is correlated with the mean temperature of the surface—680 hPa layer, which crudely approximates the cloud temperature. These data apply to the region from 60°N to 60°S and show that in the warmest regions of the globe a decrease in W is correlated with an increase of temperature. This result is similar to the optical depth sensitivities deduced by Tselioudis et al. (1992) who argue that specific regional changes in the optical depth-temperature correlation is more complex than one simply defined by thermodynamical considerations.

The relationship between LWP and cloud albedo can be examined using global SSM/I information and cloud albedo available from ERBE. While this is an important task, it has been difficult to find enough coincident data to carry out correlations between albedo and LWP—a problem that will be rectified with the launch of NASA's Tropical Rainfall Measurement Mission (TRMM) in 1997. Nevertheless a limited match of SSM/I and ERBE was presented in the study of Greenwald et al. (1995) in which the albedo of low overcast clouds as determined by ISCCP is presented as a function of LWP (Fig. 7.13b). The curves shown represent relations derived from theory assuming different values of r_e. Possible reasons for differences between theory and observation as shown need to be explored and explanations vary from biases introduced in sampling the different data to macroscopic effects that dramatically alter the intrinsic relationship between albedo and LWP.

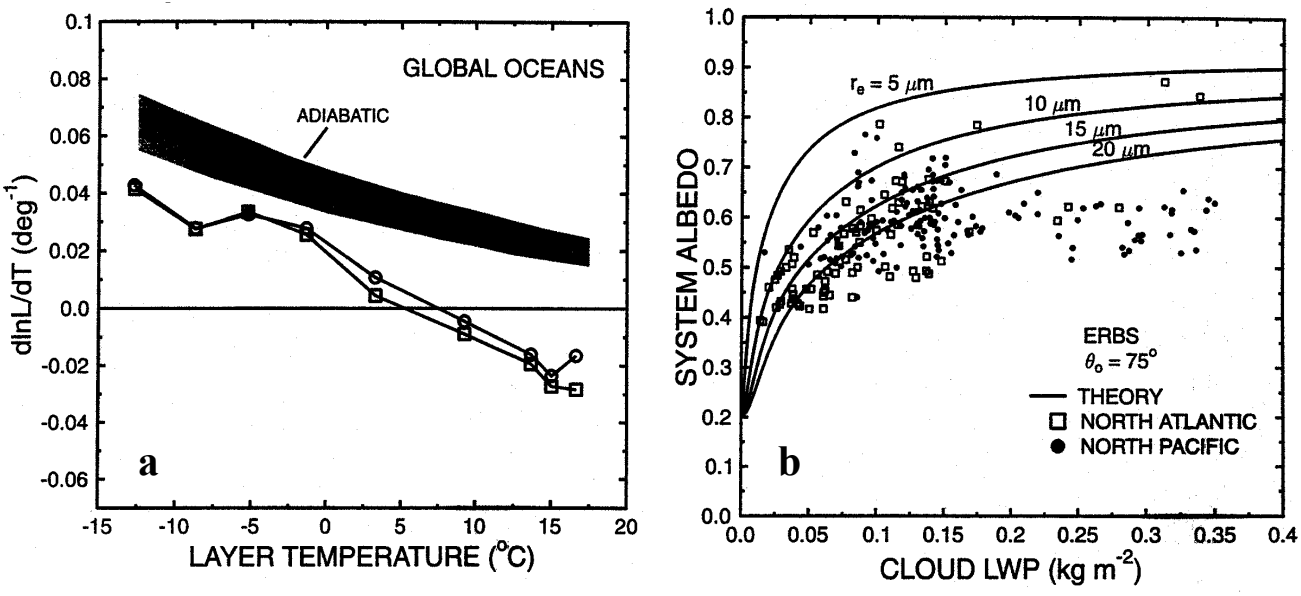

Fig. 7.13 (a) Global observations between f versus temperature (C) of the atmospheric layer between the surface and 680 hPa. Observations using composite ISCCP and microwave liquid water are given by symbols and the light shading indicates the range of the relationship derived from adiabatic assumptions for clouds of varying thickness and height. (b) Scatter diagram of the instantaneous albedo measurements from ERBs at a solar zenith angle of 75° versus coincident SSM/I LWP data for low clouds over the Northern Pacific and Atlantic during June and July 1988. Also shown are relationships based on parameterized theory for different values of r_e (Greenwald et al., 1995).

(c) Net Radiation and Reciprocity

One of the curiosities of the flux difference analyses post ERBE is the near reciprocity between longwave and shortwave effects over the tropics. We can begin to explore this reciprocity in the following way. Consider the following

$$\frac{dC_{net}}{d\mathcal{W}} = \frac{dC_{SW}}{d\mathcal{W}} + \frac{dC_{LW}}{d\mathcal{W}} \tag{7.8}$$

where $\mathcal{W}$ is some unspecified cloud parameter. To help fix ideas, we might think of $\mathcal{W}$ as the cloud liquid water path W or cloud fraction N or some combination of these such that some given increase in this parameter leads to more negative values of C_{SW} and larger values of C_{LW}. For example, Fig. 7.14a presents a scatter plot of C_{net} as a function of satellite liquid water path for the mid-latitudes and tropics.

The results for the two regions appear to be fundamentally different with an apparent change in sign if rearrange Eqn. (7.8) to obtain

$$C_f = \frac{dC_{net}}{dC_{LW}} = \frac{dC_{SW}}{dC_{LW}} + 1. \tag{7.9}$$

In this expression, dC_{SW}/dC_{LW} is the change in C_{SW} with respect to C_{LW}. Over ocean regions it is reasonable to suppose that these changes arise primarily from large-scale changes in cloudiness and

perhaps large-scale changes in cloud water. The interpretation of the right-hand side of Eqn. (7.9) is as follows,

$$C_f = \begin{cases} > 0 & \text{greenhouse effect dominates,} \\ 0 & \text{greenhouse and albedo effects cancel,} \\ < 0 & \text{albedo effect dominates.} \end{cases}$$

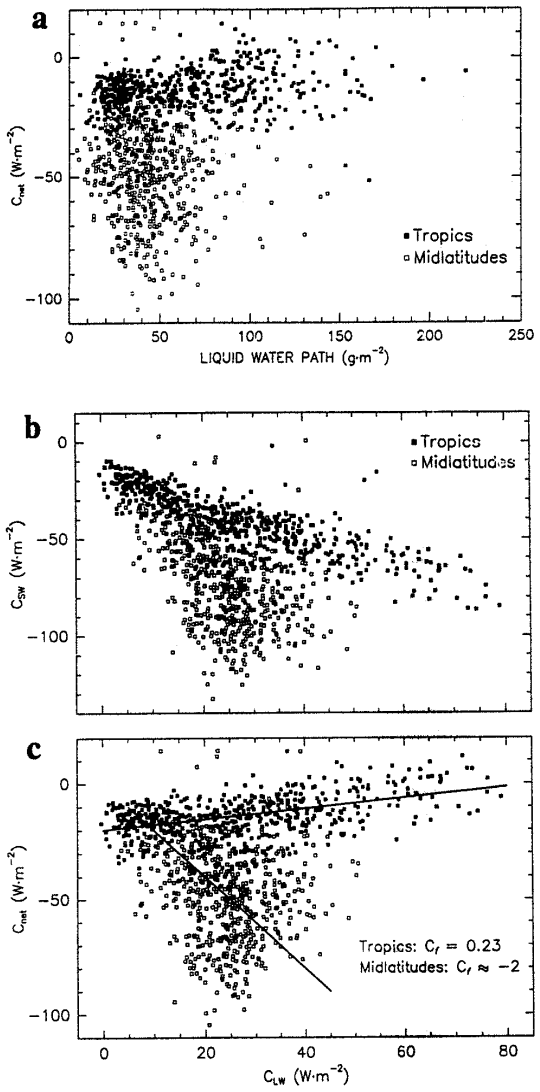

Fig. 7.14 (a) Scatter diagram of an annual composite of C_{net} versus W for the tropics (filled squares) and mid latitudes (open squares) using the Nimbus-7 ERB flux data. (b) Scatter diagram of C_{SW} versus C_{LW} for the tropics (filled squares) and mid latitudes (open squares) using the Nimbus-7 ERB flux data. The negative correlation indicates the general reciprocoal influence of clouds on the shortwave and longwave components of the ERB. (c) Scatter diagram of C_{net} and C_{LW} for the same data used in (a). The slope of a linear correlation between these flux quantities defines C_f and estimates of C_f are given.

An estimate of C_f may be obtained from plots of C_{net} and C_{LW} data presented in the manner shown in Figs. 7.14b and c. The negative correlation of C_{SW} and C_{LW} is indicative of the reciprocity of cloud effects on the ERB. The results indicate that a given change in C_{LW} (the greenhouse effect) is associated with a change in C_{SW} (the albedo effect) that is smaller for tropical clouds than observed for mid-latitude clouds. From the slope of the relationship between C_{net} and C_{LW} of Fig. 7.14c we deduce a value of C_f and therefore establish the combined impact of the greenhouse and albedo effects of clouds on the net radiation budget. We estimate $C_f = 0.23$ for tropical clouds, indicating that a change in the greenhouse effect is more dominant than the compensating change in albedo effect although the results are scattered and shows largely a reciprocity. On the other hand, $C_f \approx -2$ for mid-latitude clouds, which implies that the albedo changes dominate the net radiation balance. The result of Fig. 7.14c is consistent with the notion that the differences in the response of the ERB to tropical clouds versus mid-latitude clouds relates to the differences in the ERB attributed to large-scale changes in cloud liquid water. The greenhouse changes associated with changes in LWP cannot be completely neglected as previous cloud water feedback studies have assumed (e.g., Sommerville and Remer, 1984; Paltridge, 1980, and others).

7.6 Clouds and the Surface and Atmospheric Budget

Although the net radiative effect of clouds at the top of the atmosphere is small throughout most of the low latitudes (e.g., 7.15a and b), the partitioning of this effect between the atmosphere and the surface is both large in magnitude and opposite of sign. This is evident in the model results presented in Figs. 7.15c and d which show the distributions of the net flux differences within the atmosphere (this will be referred to as the atmospheric cloud radiative forcing, ACRF) and at the surface (the surface cloud radiative forcing) for the same GCM climate model simulations used to produce the TOA distributions presented in Fig. 7.15b. These simulations show how clouds radiatively heat the atmospheric column (relative to the clear sky) and how this heating is largely compensated by a cooling at the surface (e.g., Slingo and Slingo, 1988). The heating of the atmosphere by clouds is important for a number of reasons. The location of the maximum heating of the ACRF coincides with the maximum of deep convection and convective heating. The coupling of these different forms of heating and feedbacks between them are mentioned in more detail below.

Estimating the proportional effect of clouds on the radiative balance of the atmosphere and surface is crucial for understanding links between clouds and other components of the climate system. For instance, both the heating of the atmosphere and the cooling at the Earth's surface (specifically the ocean) by clouds are key elements of hypothesized cloud-climate feedback mechanisms (Randall et al., 1989; Ramanathan and Collins, 1992). Unfortunately, there are no measurements to confirm model simulations of the partitioning of the cloud radiative forcing between the atmosphere and the surface and it is clear that more detailed information about the surface radiation budget is required to do this.

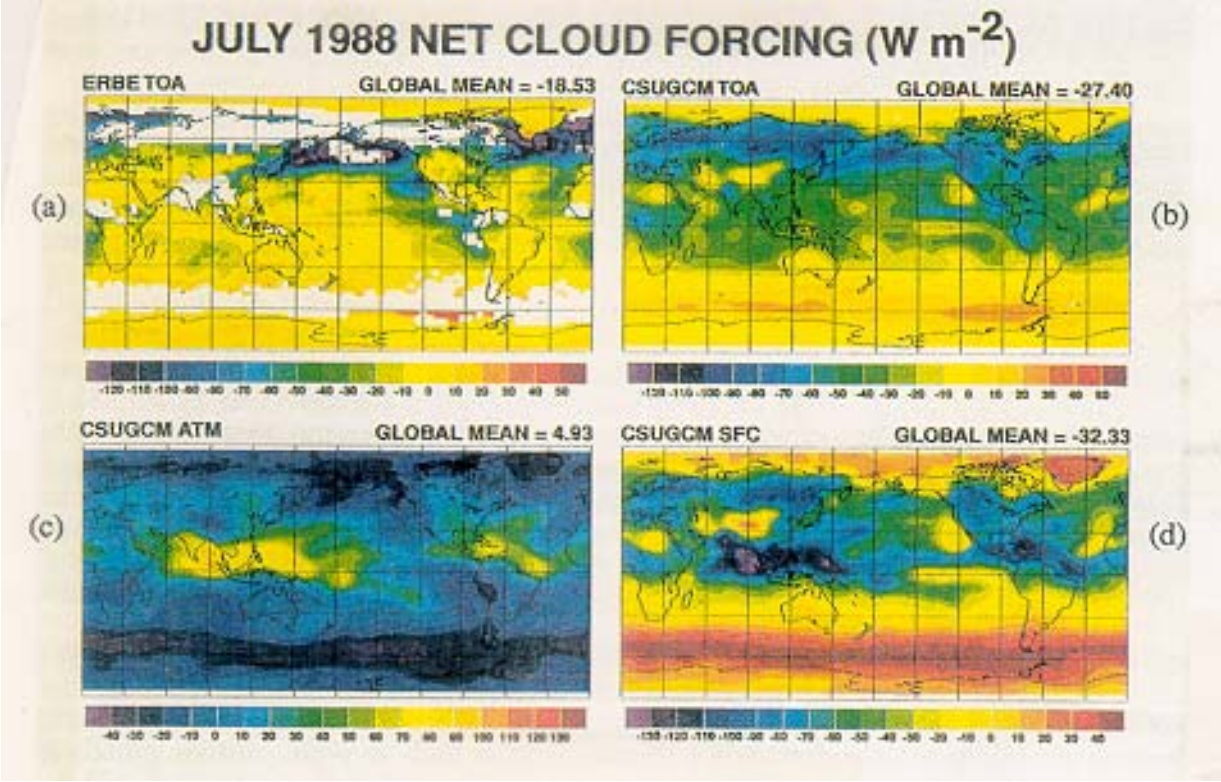

Fig. 7.15 Net cloud-radiative forcing for July 1988 (all numbers are in W m^{-2}). (a) The TOA forcing derived from ERBE. (b) A GCM model comparison. (c) The forcing derived from model simulations for the atmosphere, and (d) surface.